Vacuum 212 (2023) 112049

Contents lists available at ScienceDirect

Vacuum

journal homepage: www.elsevier.com/locate/vacuum

High-temperature stability core-shell engineered Ti_3AlC_2@C@SiO_2 for excellent microwave absorbing properties

Yang Guo [a], Xiaoying Guo [a,*], Xian Jian [b]

[a] School of Electrical and Information Engineering, University of Panzhihua, Panzhihua, 617000, China
[b] School of Materials and Energy, University of Electronic Science and Technology of China, Chengdu, 611731, China

ARTICLE INFO

Handling Editor: Prof. L.G. Hultman

Keywords:
Ti_3AlC_2
Core-shell engineering
High-temperature stability
Microwave absorption properties

ABSTRACT

Layered structure Ti_3AlC_2 (TAC) has good thermal stability and excellent electrical conductivity, which is expected to be a great high-temperature electromagnetic microwave absorber. Herein, we derive TAC@C@SiO_2 composites by catalytic chemical vapor deposition (CCVD) technology and Stöber process. Core-shell engineering can accomplish a mass loss of just 0.20% at 500°C for 1 h. An outstanding microwave absorption performance can be achieved with a minimum reflection loss of −31.63 dB and the maximum absorption bandwidth of 2.08 GHz at the matching thickness of 2.0 mm with the synergistic effect of abundant polarization mechanism and multiple scattering. Additionally, this research can serve as a guide for the utilization of TAC in the field of high-temperature microwave absorption materials, and can also provide suggestions for the design of environment-adaptable core-shell absorbers.

1. Introduction

Electromagnetic waves (EMWs) are now widely employed as a medium for wireless control and information on electronic equipment in detection, positioning, and communication [1–3]. Naturally, the derived electromagnetic pollution (electromagnetic radiation and electromagnetic interference) has become the focus due to the harm to human organs and the failure of electronic equipment [4,5]. Microwave-absorbing materials (MAMs) can attenuate EMWs and convert them into heat or other forms of energy, which are employed as an important way to address electromagnetic pollution [6,7].

Extreme application situations, such as those with high temperatures, high humidity heat, and salt spray conditions, need MAMs with not only exceptional microwave absorption performances (MAPs), but also additional functional features (e.g., oxidation and corrosion resistance) [8,9]. MAMs with good high-temperature stability can be employed in the aero engine's heat shield and tailpipe, which is the central piece in the multi-functional absorption material field [10,11]. X Jian et al. prepared FeSiAl@SiO_2@Al_2O_3 composite structure by plasma induction technique [12]. It exhibited good high-temperature oxidation resistance with the oxidation starting temperature up to 1279 °C. The minimum reflection loss (RL_{min}) was −46.29 dB at 16.93 GHz with a thickness of 2.0 mm. The maximum absorption bandwidth (*MAB*) was up to 7.33 GHz (<−10 dB) at a matched thickness of 2.5 mm. Nevertheless, it is hardly possible for magnetic materials to exert magnetic loss at high temperatures due to the Curie temperature limitation [13]. Z Y Jiang et al. created temperature-insensitive reduced graphene oxide@-carbon spheres through the design of the structure and composition [14]. The *MAB* of the carbon-based composites with 3.0 wt% reduced graphene oxide@carbon could cover the entire X-band ranging from 20 to 200°C. However, the poor high-temperature stability of carbon-based materials at over 400°C limits their promotion in the field of high-temperature microwave absorption [15]. Spray drying and 3D printing technologies were used to create SiC nanowires (SiC_{nw})/SiC whiskers (SiC_w) foam with a "wire-on-sphere" hierarchical structure [16]. At room temperature, the *MAB* and RL_{min} of SiC_{nw}/SiC_w foam could reach 4.0 GHz and −57.0 dB, respectively. At 600°C, the *MAB* and RL_{min} were 3 GHz and −15 dB, respectively. SiC_{nw}/SiC_w foam may retain *MAB* ranging from 2.7 to 3.9 GHz and RL_{min} ranging from −16.0 dB to −64.0 dB even after being oxidized at 1000–1500°C. However, the complex preparation process setup severely restricts the widespread use of SiC-based composites [17]. It follows that finding or creating a microwave-absorbing material with good high-temperature stability is still required.

Ti_3AlC_2 (TAC) is an essential candidate for high-temperature MAMs because of their particular layered structure, good high-temperature

* Corresponding author.
E-mail address: [redacted] (X. Guo).

https://doi.org/10.1016/j.vacuum.2023.112049
Received 27 February 2023; Received in revised form 23 March 2023; Accepted 25 March 2023
Available online 27 March 2023

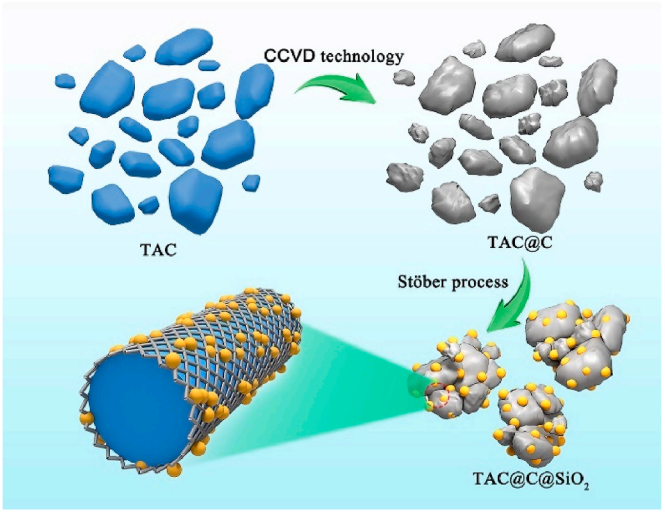

Scheme 1. Illustration of synthetic process of TAC-based composites.

thermal stability and excellent electrical conductivity [18–20]. TAC was manufactured in two steps by X Q Li et al., and also demonstrated their oxidation behavior at 1300°C [21]. The oxidation behaviour of TAC ceramics exhibited anisotropy. In addition, the textured side surface exhibits better oxidation resistance due to the rapid diffusion of Al in basal planes and the formation of an Al_2O_3 protective layer. J Li et al. fabricated Fe-doped TAC through the solid-phase reaction method [18]. The RL_{min} of Fe-doped TAC composites can achieve −33.3 dB, and the *MAB* could reach 3.9 GHz with a thickness of only 1.5 mm. Despite this, preparing high-temperature stability and good MAP of TAC is still a problem.

Herein, we propose a novel approach for creating a high-temperature stable electromagnetic absorbent that takes advantage of component synergy and seeks to address this problem. To this end, TAC@C@SiO_2 composites with beneficial high-temperature stability and MAP were prepared by catalytic chemical vapor deposition (CCVD) technology and Stöber process. Core-shell engineering can help TAC achieve a mass loss of only 0.2% at 500°C for 1 h. With a good polarization mechanism and multiple scattering synergies, good MAP can be achieved with a minimum reflection loss of −31.63 dB and the widest absorption bandwidth of 2.08 GHz at a matched thickness of 2.0 mm. This work provides a reference for the design of high-temperature stable, and efficient microwave-absorbing TAC-based materials.

2. Experimental

2.1. Materials

TAC (99.0%) was obtained from Nanjing Mingchang New Material Technology Co. Ltd. It was prepared by the high-temperature solid-state sintering process. Tetraethyl orthosilicate (TEOS, 99.0%), ammonia solution (25.0 wt%) and absolute alcohol (99.7%) were all obtained from Chengdu Jinshan Chemical Reagent Co. Ltd.

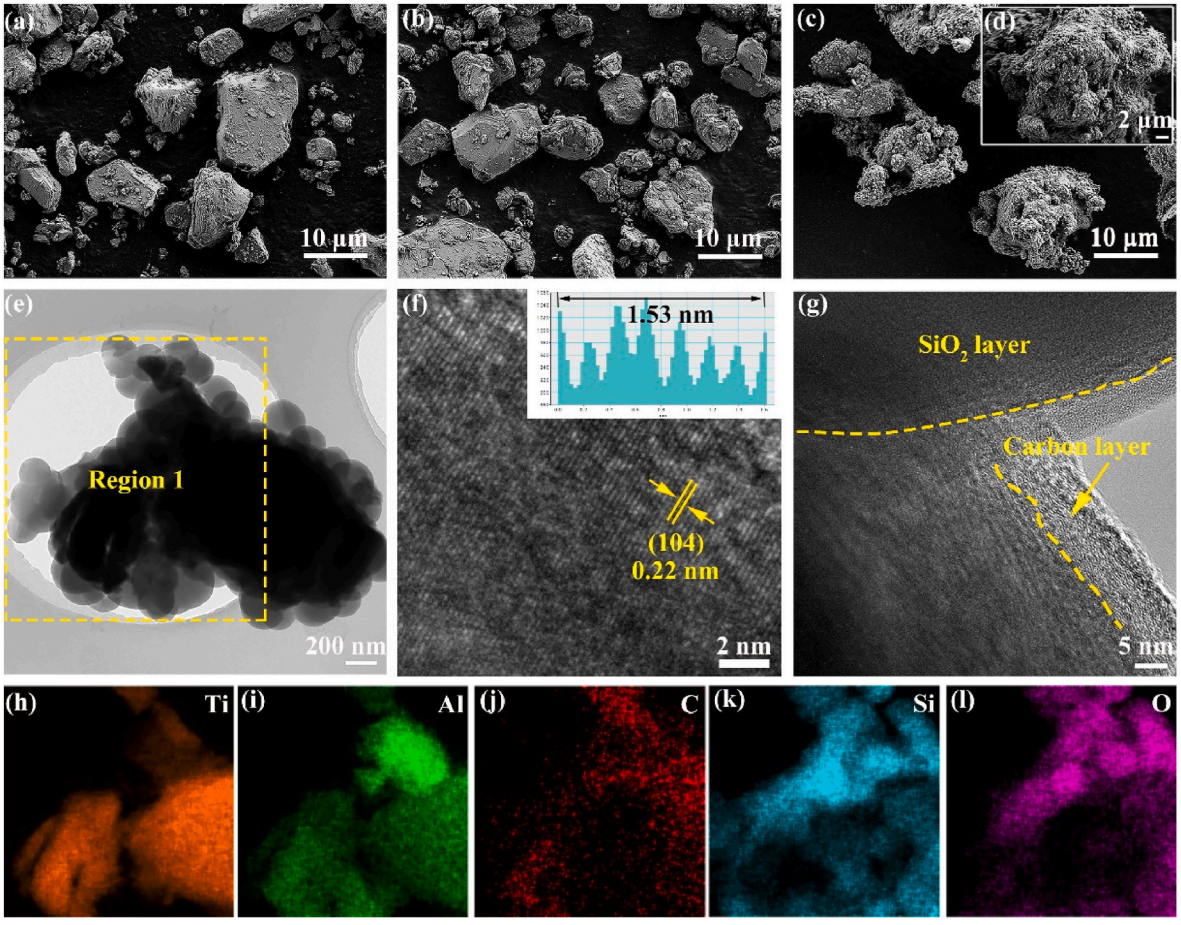

Fig. 1. SEM images of (a) TAC, (b) TAC@C, (c–d) TAC@C@SiO_2. (e) TEM image of TAC@C@SiO_2 and (f–l) the corresponding elemental mapping distribution of region 1 in (e). (f–g) HRTEM images of TAC@C@SiO_2 (inset: Contrast intensity profile in f).

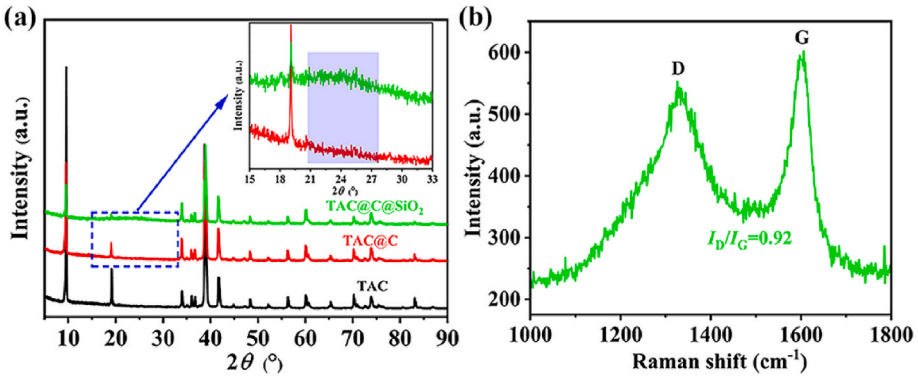

Fig. 2. (a) XRD patterns of TAC, TAC@C, and TAC@C@SiO_2. (b) Raman shfits of TAC, TAC@C, and TAC@C@SiO_2.

2.2. Synthesis of TAC@C

As depicted in Scheme 1, the TAC was treated by CCVD technology and a carbon layer was grown on its surface. In detail, TAC was initially placed in a quartz boat in the middle position of the tube furnace. The temperature was then raised to 650 C while being shielded by Ar at a rate of 10°C/min. Afterwards, acetylene (C_2H_2) was introduced into the tube furnace at a flow of 40 mL/min for 15min at 650°C. The tubular furnace was finally cooled to room temperature, and the sample obtained was given the name TAC@C.

2.3. Preparation of TAC@C@SiO_2

A mixture of 100 mL absolute alcohol, 25 mL deionized water, and 2.67 mL ammonia solution was agitated at 30°C for 10 min. After this, 10 g TAC@C was added to the above-mixed solution, which was continuously stirred for 10 min to form a pre-hydrolysis solution. Finally, 33 mL TEOS was dropwise added into the pre-hydrolysis solution and stirred for 8 h. The TAC@C modified by TEOS were named TAC@C@SiO_2.

2.4. Characterization

The surface micromorphology of all samples was examinded by a scanning electron microscope (SEM, Ultra plus, Germany) with an acceleration voltage of 15 kV. X-ray diffraction (XRD) patterns were achieved in the implementation of an Ultima (Rigaku, Japan) diffractometer, using Cu Kα radiation (λ = 1.5406 Å) with a scanning rate of 5°/min. Transmission electron microscopy (TEM) images were collected in an FEI Tecnai G2 F20 X-Twin. Raman shift of all samples was gleaned through using a thermo DXR2xi (USA) with a 532 laser. The surface chemical composition and group distribution of TAC-based samples were analyzed by X-ray Photoelectron Spectrum (XPS, Thermo Scientific Nexsa, USA) under ultra-high vacuum using a monochromated Al Ka X-ray source (hυ = 1468.68 eV). The working voltage was 12.0 kV. The electron emission angle was 58°, and the analysis area was 400*400 μm. The binding energies of all samples were calibrated by reference to the work function of TAC with a value of 4.78 eV [20]. From the literature [22,23], the sum of C 1s binding energy and the work function of TAC is fixed at 289.58 ± 0.14 eV, allowing the C 1s value to be estimated from the work function value. The C 1s value was used to calibrate the XPS spectra of other elements. Thermogravimetric (TG) analysis of the TAC-based composites was obtained on an STA 449 F3 simultaneous thermal analysis (Netzsch, Germany), under airflow (20 mL/min) with a heating rate of 10 °C/min between 30 and 1300 °C. According to the mass ratio of 4:1, the TAC-based composites and paraffin are uniformly mixed, and pressed into a ring sample with a 3.0 inner diameter and a 7.0 outer diameter. The electromagnetic characteristics were tested by a vector network analyzer (N5230A, Agilent, USA) through a coaxial approach between 0.5 and 18.0 GHz.

3. Results and discussion

The surface morphology of all samples was observed by SEM. The SEM image of TAC is given in Fig. 1(a), which is an irregular polyhedron structure. The surface morphology of TAC after undergoing CCVD technique has no significant change, as shown in Fig. 1(b). After being treated by Stöber process, the surface of TAC is surrounded by a large number of spherical SiO_2 nanoparticles, as displayed in Fig. 1(c). Fig. 1 (d) shows a partial magnification of Fig. 1(c). It is discovered that the agglomeration of TAC@C@SiO_2 nanoparticles occurred. The phenomenon may have been brought on by the change in the substrate's surface polarity due to the bonding of the silane groups and the dangling bonds of the deposited SiO_2 nanoparticles [24]. In particular, the dimension of TAC@C@SiO_2 is significantly larger than that of TAC. The interface and crystal structure of TAC@C@SiO_2 are further displayed in the high-resolution TEM (HRTEM) images, as depicted in Fig. 1(e–g). Fig. 1 (e) shows that spherical SiO_2 nanoparticles were evenly dispersed across the surface of TAC. The lattice spacing in Fig. 1(f) is 0.22 nm, which match with the (104) crystal planes of the TAC. At the same time, it can be clearly seen that the carbon layer deposited on the surface of TAC is amorphous with a thickness of about 5 nm. The amorphous carbon layer and TAC have excellent atomic-level cohesiveness, according to their interfacial lattice. Moreover, it is discovered that the 200 nm-thick SiO_2 layer produced on the surface of TAC@C is amorphous as well. The amorphous carbon and SiO_2 layer can induce a significant number of interfaces and form a "micro capacitor" structure, which is helpful for enhancing impedance matching and producing interface polarization [25]. The element mapping images of region 1 for TAC@C@SiO_2 verify that Ti, Al, C, Si, and O were distributed uniformly, as shown in Fig. 1 (h–l).

The crystal structure of all samples was analyzed by XRD. Fig. 2(a) demonstrates the characteristic peaks of TAC (PDF#52–0875) that are positioned at 9.5°, 19.2°, 33.7°, 36.8°, 39.0°, 41.8°, 48.5°, 56.6°, 60.3°, 70.6°, 74.1°, and 83.5°.These peaks correspond to the (002), (004), (100), (103), (104), (105), (107), (109), (110), (200), (118), and (0016) crystal planes of TAC, respectively. The CCVD technology and the Stöber process have little effect on the TAC's distinctive diffraction peaks. Diffraction peaks attribute to amorphous carbon can be seen in addition to the typical characteristic peaks obtained for TAC [26], as seen in the inset in Fig. 2(a). Due to the amorphous form of SiO_2, the characteristic diffraction of SiO_2 is not observed [27]. No significant characteristic peaks of impurities are found in all XRD patterns, confirming that no additional impurity phases were introduced during the production of TAC@C@SiO_2. Fig. 2(b) shows the Raman peaks of TAC@C. The distinct D and G peaks are noted in TAC@C. Here, the ratio of the intensity (I_G/I_G) obtained for the D and G peaks is 0.92, indicating a high degree of graphitization of the carbon layer. The carbon layer facilitates the

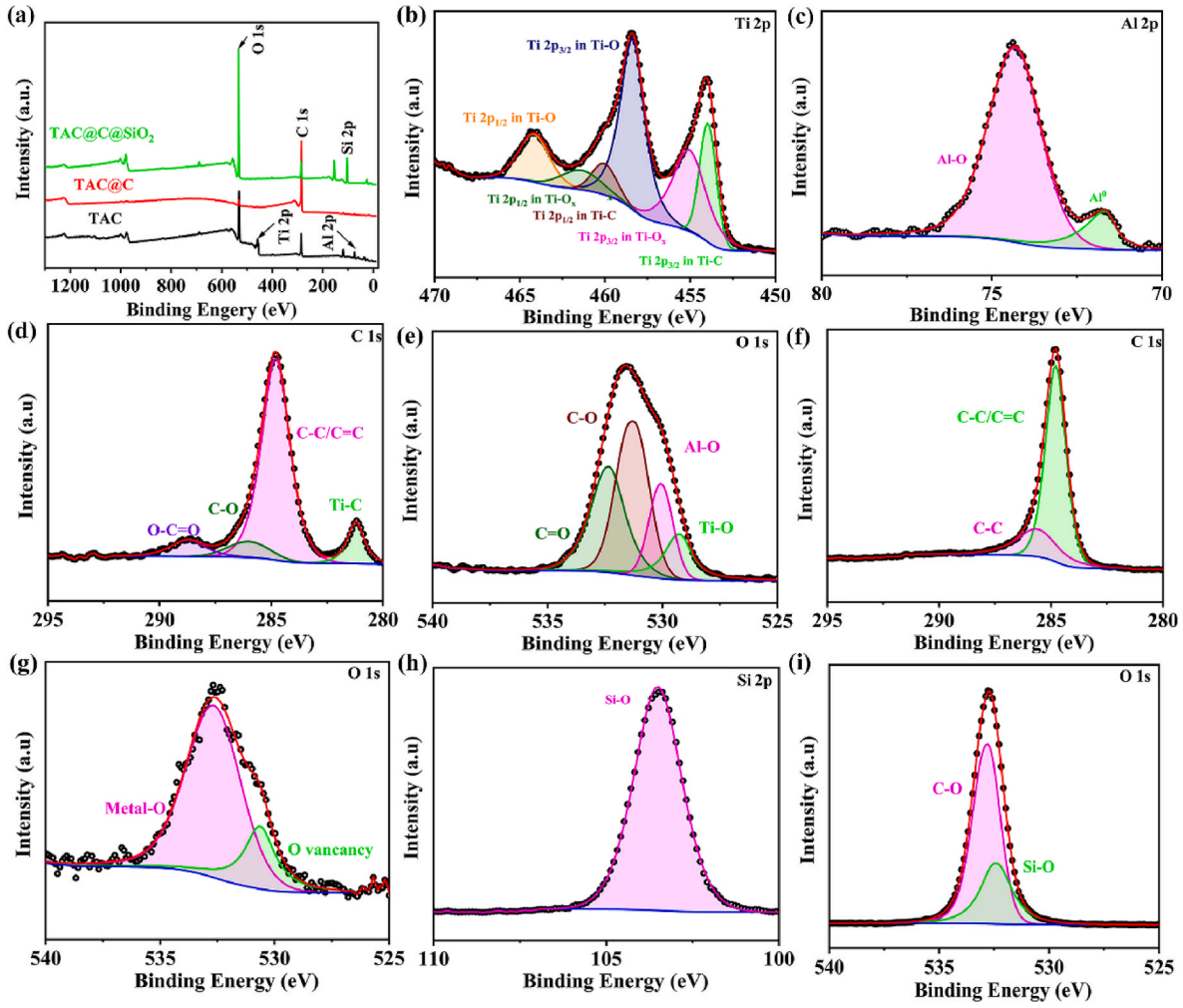

Fig. 3. (a) XPS survey spectrum of TAC, TAC@C, and TAC@C@SiO2.High–resolution XPS spectra of (b)Ti 2p, (c) Al 2p, and (d) C 1s, and (e) O 1s in TAC. High–resolution XPS spectra of (f) C 1s, and (g) O 1s in TAC@C. High–resolution XPS spectra of (h) Si 2p, and (i) O 1s in TAC@C@SiO_2.

formation of conductive networks and the construction of heterogeneous interfaces [27]. Moreover, the carbon layer's defects may function as dipole polarization centers [28].

To further expose the TAC surface's composition and elemental valence states after the treatment with catalytic chemical vapor deposition and Stöber process, all samples were subjected to XPS analysis, as shown in Fig. 3(a–i). Fig. 3(a) shows the XPS survey spectrum, which confirms the existence of Ti, Al, C, O, and Si elements. For TAC, in high-resolution XPS spectra of Ti 2p (Fig. 3(b)), the characteristic peaks at 454.1 eV, 455.1 eV, 458.4 eV, 460.2 eV, 461.6 eV and 464.3 eV are associated with Ti $2p_{3/2}$ in Ti–C, Ti $2p_{3/2}$ in TiO_x ($0 < x < 1$), Ti 2p3/2 in TiO_2, Ti $2p_{1/2}$ in Ti–C, Ti $2p_{1/2}$ in TiO_x, and Ti $2p_{1/2}$ in TiO_2, respectively [29–31]. The appearance of two Ti–O bonds indicates that Ti was oxidized during the preparation of TAC; secondly, Ti atoms inside the Ti monomer only partially interact with oxygen [32]. The presence of Ti–C bond confirms that the matrix is TAC. From the high-resolution spectrum of Al 2p (Fig. 3(c)), the characteristic peaks locate at 71.6 eV and 74.4 eV correspond to Zero-valent aluminium [33] and Al–O [34],

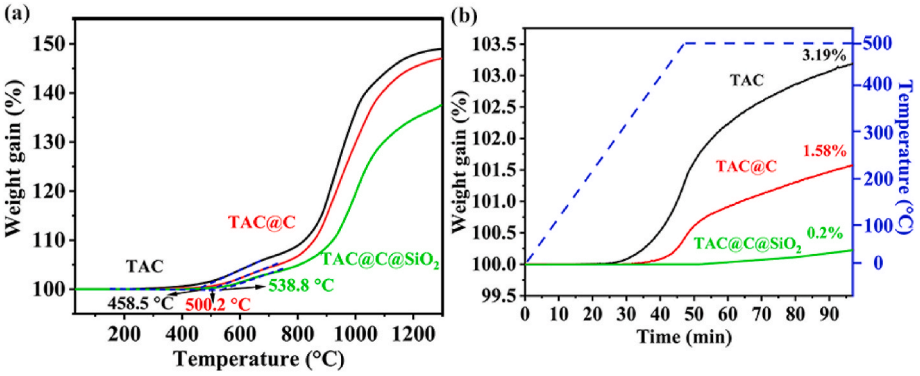

Fig. 4. (a)TG and (b) isothermal TG curves at 500°C for 1 h of TAC, TAC@C, and TAC@C@SiO_2, respectively.

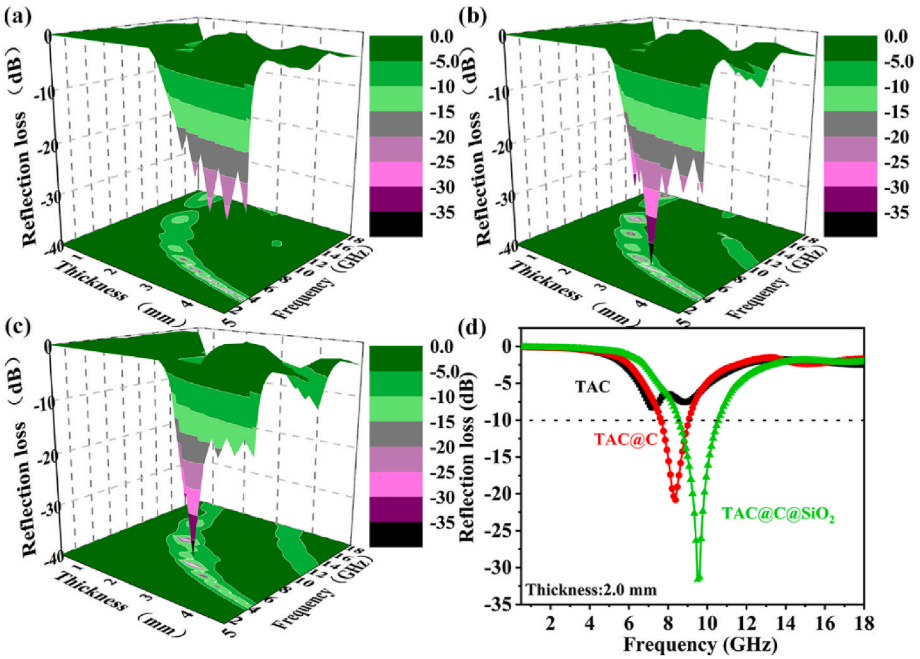

Fig. 5. 3D (three dimensional) RL maps in the frequency of 0.5–18 GHz for (a) TAC, (b) TAC@C and (c) TAC@C@SiO_2. (d) RL curves of TAC, TAC@C, and TAC@C@SiO2 with a thickness of 2.0 mm.

respectively. In the high-resolution XPS spectrum of C 1s (Fig. 3(d)), four distinctive peaks can be observed at 281.2 eV, 284.8 eV, 286.1 eV and 288.8 eV, corresponding to Ti–C, C–C/C═C, C–O and O–C═O [35], respectively. The O1s XPS spectrum of TAC confirms the presence of TiO_2 and Al_2O_3, as shown in Fig. 3(e). According to the high-resolution spectrum of C 1s (Fig. 3(f)) for TAC@C, the peaks at 284.8 and 285.7 eV are assigned to C–C/C═C and C–C, respectively [36]. This demonstrates that carbon is present on the TAC surface. The peaks at 530.7 and 532.7 eV in the O 1s high-resolution XPS spectrum (Fig. 3(g)) can be attributable to oxygen vacancies and metal-O (Ti–O/Al–O), respectively [37]. For TAC@C@SiO_2, the characteristic peak at 104.4 eV in the high-resolution XPS pattern of Si 2p corresponds to the Si–O in SiO_2 [38], as shown in Fig. 3(h). This proves that SiO_2 successfully grew on the TAC surface. The typical peaks in the high-resolution XPS spectra of O 1s (Fig. 3(i)) are in the order of Si–O and C–O [39,40], which is consistent with the findings of the high-resolution XPS mapping study of Si 2p.

High-temperature oxidation is a crucial factor affecting the stable service of high-temperature wave-absorbing materials. TG analysis measured the mass change of TAC-based composites in air from 30 to 1300 °C and the mass gain after holding at 500 °C for 1 h. The results are displayed in Fig. 4. As seen in Fig. 4(a), all samples have an increase in mass gain when oxidation-related temperature increased. By extrapolating of the TG curves [41], the onset oxidation temperatures of TAC, TAC and TAC@C@SiO_2 are determined and were 458.5°C, 500.2°C and 538.8°C, respectively. TAC@C@SiO_2 have an initial oxidation temperature of 80.3°C higher than TAC. This indicates that TAC coated carbon layer and SiO_2 layer exhibit better high-temperature oxidation resistance than the TAC at 500°C. Further, the TAC-based composites were held in air at 500°C for 1 h, as shown in Fig. 4(b). TAC@C@SiO_2 exhibits good high-temperature stability because the mass gain increase is just 0.20%, which is 3.17% lower than pure TAC. The higher high-temperature stability is ascribed to the presence of C@SiO_2 core-shell, which inhibits the oxidation activity of TAC [42]. On the other side, this may be because SiO_2 slows down the diffusion rate of oxygen on the surface of TAC [43]. In addition, the core-shell structure provides thermal protection and reduces heat transfer at high temperatures [44]. It reduces the internal materials' temperature and the chance of oxidation and corrosion. The core-shell structure provides mechanical protection against wear and damage at high temperatures.

According to equations (1-2)' [45], the relationship between the thickness and reflection loss of TAC-based materials at 0.5–18 GHz can be calculated. Fig. 5(a–c) shows the 3D reflection loss plots related to the thickness of TAC-based materials at 0.5–18 GHz.

$$Z_{in} = Z_0\sqrt{\frac{\mu_r}{\varepsilon_r}}\tanh\left(j\frac{2\pi f}{c}d\sqrt{\mu_r \bullet \varepsilon_r}\right) \quad (1)$$

$$RL(dB) = 20\log|(Z_{in} - Z_0)/(Z_{in} + Z_0)| \quad (2)$$

here, Z_{in} and Z_0 denote the input and internal impedances, respectively. The complex permeability and permittivity are represented by μ_r and ε_r, respectively. *f, d, and c* are the frequency of the electromagnetic wave, the thickness of the absorber, and the speed of light, respectively.

By comparing the *RL* values and *MAB* of the TAC-based absorbers with a thickness of 2.0 mm at 0.5–18 GHz, the MAP of TAC@C@SiO_2 has significant differences compared with TAC and TAC@C. From Fig. 4(d), the *MAB* of TAC is 0 GHz, and RL_{min} is −8.3 dB at 7.24 GHz. The *MAB* of TAC@C is 1.47 GHz at 7.64–9.11 GHz, and RL_{min} is −20.86 dB at 8.38 GHz. The *MAB* of TAC@C@SiO_2 is 2.08 GHz at 8.51–10.59 GHz, and RL_{min} is 31.63 dB at 9.51 GHz. With a significant drop in RL_{min} to 12.56 dB and an increase in *MAB* to 1.47 GHz, it can be seen that the MAP of TAC@C is somewhat better than that of TAC. There are three causes for this phenomenon: First, the surface state of the TAC is considerably altered by the core-shell C@SiO_2 structure, which further enhances the impedance matching between the matrix and free space [46]. This makes it easier for incident EMWs to penetrate the absorber's interior, where they can be lost and converted into heat energy. Second, the C@SiO_2 structure that was deposited produces many interfaces in the TAC. The abundant interfaces induce and enhance many loss mechanisms, including space charge polarization relaxation, interfacial polarization relaxation, and dipole polarization relaxation. Amorphous carbon flaws can act as polarization centers and cause dipole polarization to relax. The contact between TAC/C/SiO_2 is capable of experiencing interfacial polarization relaxation. Finally, incident EMWs inside the absorber may reflect and scatter more often due to the interfaces present in the TAC@C@SiO_2 [47]. Also, it is encouraged that the

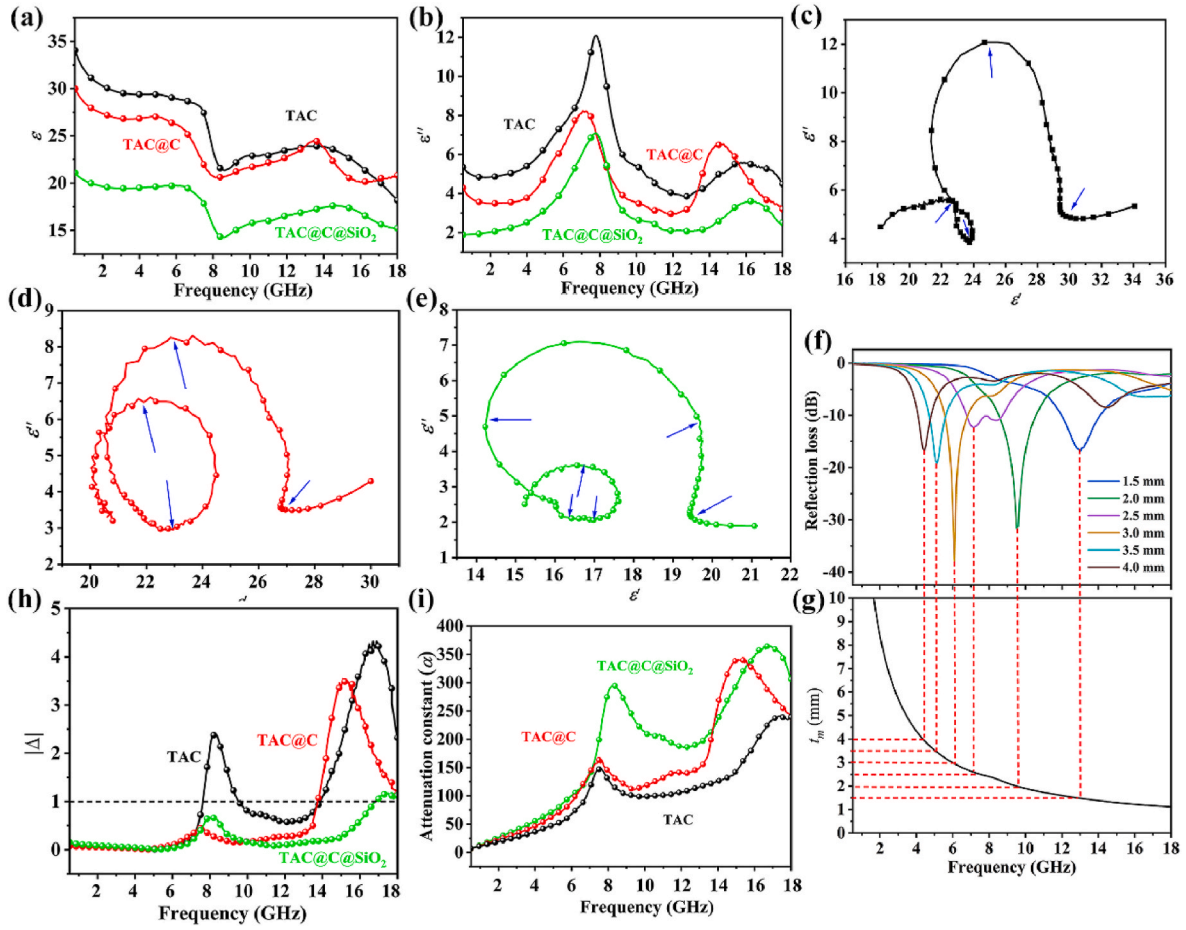

Fig. 6. (a) Real part and (b) imaginary part of complex permittivity of TAC–based composites. Cole–Cole curves of (c) TAC, (d) TAC@C and (e) TAC@C@SiO_2. Frequency dependence of (e) variable RL values and (f) simulated thickness for TAC@C@SiO_2. (h) Impedance mismatch degree curve at a thickness of 2.0 mm and (i) attenuation constant of TAC, TAC@C, and TAC@C@SiO_2.

absorption component loses EMWs. The defects in the amorphous carbon layer can act as scattering points for multiple scattering of electromagnetic waves and consume electromagnetic wave energy.

The MAP of TAC-based composites is usually analyzed according to the complex permittivity ($\varepsilon_r = \varepsilon' - j\varepsilon''$). As illustrated in Fig. 5(a), the ε' of TAC gradually declines from 34.12 to 17.99 with increasing frequency. ε' of TAC@C gradually decreases from 29.97 to 20.90. ε' of TAC@C@SiO_2 gradually decreases from 20.95 to 15.30. It is mainly because the amorphous carbon layer and SiO_2 layer have fewer moving electrons, which can effectively reduce the electrical conductivity of TAC. All samples exhibit typical dielectric response characteristics. The TAC@C@SiO_2 has a lower value of ε', which is related to the presence of the C and SiO_2 layers. In addition, the ε'' of the TAC coated with C@SiO_2 layer decreases from 5.42 to 1.87 with increasing frequency and from 4.54 to 2.48, as shown in Fig. 6(b) where ε' denotes the capacity to store electrical energy and ε'' denotes the ability to lose electrical energy. A lower ε'' implies a lower capacity for electrical energy loss. However, multiple fluctuations of the sample with increasing frequency can also be observed in Fig. 6(a), which implies a significant polarization behavior in attenuating the incident EMWs. This could result from dipole polarization happening on material flaws or functional groups, as well as interfacial polarization brought on by charge accumulation on the inhomogeneous junction's surface [48]. In brief, both polarization patterns enhance the absorber's dielectric loss ability.

Debye relaxation is the main way to show the dielectric loss of MAMs [49,50]. Usually, Debye relaxation can be represented by a Cole-Cole curve. According to equations (3)–(5), the correlation between ε' and ε'' can be expressed as follows [51,52]:

$$\varepsilon' = \varepsilon_\infty + \frac{\varepsilon_s - \varepsilon_\infty}{1 + (2\pi f)^2 \tau^2} \tag{3}$$

$$\varepsilon'' = \frac{2\pi f \tau (\varepsilon_s - \varepsilon_\infty)}{1 + (2\pi f)^2 \tau^2} \tag{4}$$

$$\left(\varepsilon' - \frac{\varepsilon_s - \varepsilon_\infty}{2}\right)^2 + (\varepsilon'')^2 = \left(\frac{\varepsilon_s - \varepsilon_\infty}{2}\right)^2 \tag{5}$$

here, τ stands for polarization relaxation time, ε_s for static permittivity, and ε_∞ points to the high-frequency limited permittivity.

As shown in Fig. 6(c–e), more semicircles can be observed in the Cole-Cole diagram of TAC@C@SiO_2, meaning more relaxation processes occur. The mutual coupling induces more relaxation processes from the TAC, C and SiO_2 layers [53] In addition, a variable number of semicircles can be seen in other samples, which proves the prevalence of Debye relaxation processes in TAC.

In general, the position of the strongest absorption peak can be adjusted to lower frequencies by increasing the thickness of MAMs. This can be explained by the quarter-wavelength resonance equation $f_m = [(2k-1)c]/(4t_m n)$ [54], where f_m is the resonant frequency, t_m is the resonant thickness, k is a positive integer, and $n = \mathrm{Re}(\sqrt{\varepsilon_r \mu_r})$ is the refractive index of the composite. Fig. 6(f and g) shows the plot of *RL* values versus simulated thickness for TAC@C@SiO_2. It can be clearly implied that the reflection loss curves of TAC@C@SiO_2 are in good agreement with the quarter-wavelength theory.

The impedance mismatch degree is also critical in determining the

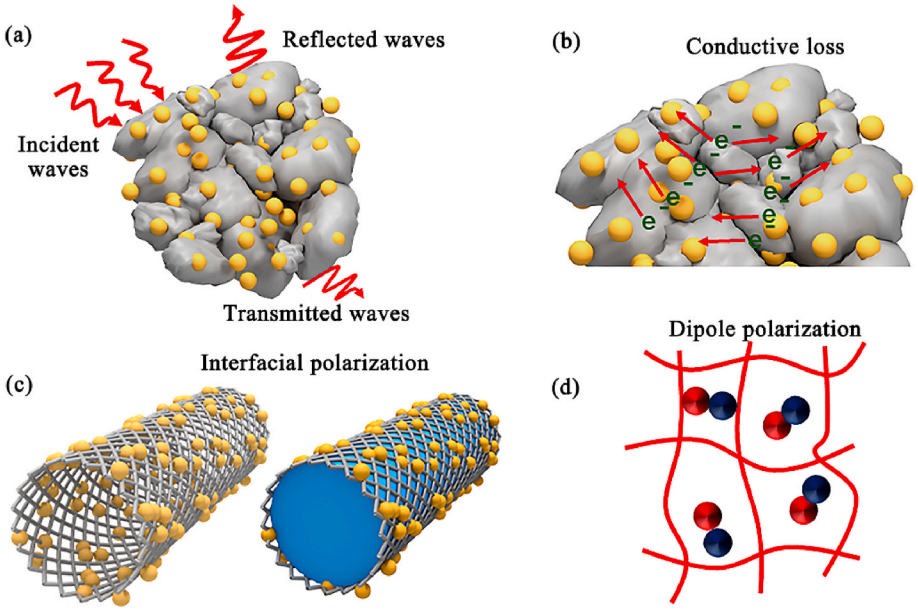

Fig. 7. EMW absorption mechanism of TAC@C@SiO_2

MAP of MAMs. According to Eqs. (7-8)' [55], we can get the relationship between $|\Delta|$ and frequency at a thickness of 2 mm, as shown in Fig. 6(h).

$$|\Delta| = \left|sin\, h^2(Kfd) - M\right| \tag{6}$$

here, h denotes the Planck constant. K and M can be determined by the complex permittivity and complex permeability of the MAM.

$$K = \frac{4\pi\sqrt{\mu'\varepsilon'}\, sin\frac{\delta_e}{\delta_m}}{ccos\delta_e\, cos\,\delta_m} \tag{7}$$

$$M = \frac{4\mu'\, cos\,\delta_e\varepsilon'\, cos\,\delta_m}{(\mu'\, cos\,\delta_e - \varepsilon'\, cos\,\delta_m)^2 + \left[tan\left(\frac{\delta_m}{2} - \frac{\delta_e}{2}\right)\right]^2(\mu'\, cos\,\delta_e + \varepsilon'\, cos\,\delta_m)^2} \tag{8}$$

in general, the $|\Delta|$ value of EMW is close to 0, which indicates the easier-to-incident EMWs [56]. Compared with TAC and TAC@C, TAC@C@-SiO_2 has the lowest $|\Delta|$ value and is less than 1 at 0.5–16.5 GHz. This indicates that TAC and TAC@C have poor impedance matching and deteriorate the ability to absorb incident EMWs.

According to the transmission line theory, the attenuation constant (α) can be calculated by Equation (9), which reflects the attenuation capability of the MAM [57,58]. Fig. 6(h) shows each sample's correlation curves of attenuation coefficients versus frequency. Each curve has a significant change with increasing frequency. Meanwhile, the attenuation system of TAC@C@SiO_2 is more prominent than the other samples, which indicates that TAC@C@SiO_2 has more vital attenuation ability and MAP for incident EMWs.

$$\alpha = \frac{\sqrt{2}\pi f}{c} \times \sqrt{(\mu''\varepsilon'' - \mu'\varepsilon') + \sqrt{(\mu'\varepsilon'' + \mu''\varepsilon')^2 + (\mu''\varepsilon'' - \mu'\varepsilon')^2}} \tag{9}$$

where, μ' and μ'' are the real and imaginary parts of the complex permeability, respectively.

Fig. 7 illustrates the absorption mechanism of TAC@C@SiO_2 for EMWs, revealing how many mechanisms work together to produce their remarkable absorption capability. On the one hand, due to the large specific surface area of the coupled TAC@C@SiO_2, the conductive network is more easily constructed and completed, facilitating the absorption of EMWs (Fig. 7(b)). Inner electrons move in a specific direction due to the current induction transmission produced by the conductive network under the influence of external electromagnetic fields, making it easier to transform electromagnetic energy into heat energy [51]. On the other hand, the EMWs entering the absorber are reflected and scattered. In this process, a large number of EMWs will be attenuated. Due to the difference between TAC, C and SiO_2, electrons in the different layered media between TAC, C and SiO_2 can accumulate at the contact interface, leading to interfacial polarization, as displayed in Fig. 7(c). Thirdly, the presence of carbon defects and oxygen vacancies in the TAC@C@SiO_2 composites under the action of external electromagnetic fields will produce dipole polarization (Fig. 7(d)).

4. Conclusion

We constructed TAC@C@SiO_2 composite structures based on CCVD technology and Stöber process. Based on core-shell engineering, it is possible to achieve a mass loss of only 0.20 ± 0.01% at 500°C for 1 h. This is an improvement of 3.17 ± 0.01% compared to pure TAC. The good thermal stability is a result of the fact that the C@SiO_2 shell structure suppresses the oxidation activity of the substrate and slows down the oxygen transport rate. At a matched thickness of 2.0 mm, the RL_{min} of TAC@C@SiO_2 is −31.63 dB, and the MAB is 2.08 GHz. The good MAP originates from the multiple heterogeneous interfaces co-constructed by the core-shell C@SiO_2 structure and the substrate, generating a rich polarization mechanism and multiple scattering. This work provides a reference for the utilization of TAC materials in the field of high-temperature microwave absorbers, and also provides ideas for the exploitation of environmentally adapted shell-structured absorbers.

CRediT authorship contribution statement

Yang Guo: Writing – review & editing, Writing – original draft. **Xiaoying Guo:** Resources. **Xian Jian:** Supervision, Methodology.

Declaration of competing interest

The authors declare that they have no known competing financial interests or personal relationships that could have appeared to influence the work reported in this paper.

Data availability

Data will be made available on request.

Acknowledgment

The study is supported by funds from the National Natural Science Foundation of China (No. 52202368) and the Natural Science Foundation of Sichuan, China (Nos.2022NSFSC0347 and 2023NSFS0415).

References

[1] S. Ren, H. Yu, L. Wang, Z. Huang, T. Lin, Y. Huang, J. Yang, Y. Hong, J. Liu, State of the art and prospects in metal-organic framework-derived microwave absorption materials, Nano-Micro Lett. 14 (1) (2022) 68.
[2] B. Zhao, Y. Du, Z. Yan, L. Rao, G. Chen, M. Yuan, L. Yang, J. Zhang, R. Che, Structural defects in phase-regulated high-entropy oxides toward superior microwave absorption properties, Adv. Funct. Mater. 33 (1) (2023), 2209924.
[3] J.C. Shu, M.S. Cao, Y.L. Zhang, Y.Z. Wang, Q.L. Zhao, X.Y. Fang, S.H. Yang, Y. Qin, J. Yuan, Atomic-molecular engineering tailoring graphene microlaminates to tune multifunctional antennas, Adv. Funct. Mater. (2023), 2212379.
[4] P. Liu, T. Gao, W. He, P. Liu, Electrospinning of hierarchical carbon fibers with multi-dimensional magnetic configurations toward prominent microwave absorption, Carbon 202 (2023) 244–253.
[5] T.T. Liu, Y.H. Zhu, J.C. Shu, M. Zhang, M.S. Cao, Patterned MXene-enabled switchable health monitoring and electromagnetic protection for architecture, Materials Today Physics (2023), 100988.
[6] M. Chang, Q. Li, Z. Jia, W. Zhao, G. Wu, Tuning microwave absorption properties of $Ti_3C_2T_x$ MXene-based materials: component optimization and structure modulation, J. Mater. Sci. Technol. 148 (10) (2023) 150–170.
[7] Z. Xiang, Y. Wang, X. Yin, Q. He, Microwave absorption performance of porous heterogeneous SiC/SiO_2 microspheres, Chem. Eng. J. 451 (2023), 138742.
[8] H. Zhang, F. Cao, H. Xu, W. Tian, Y. Pan, N. Mahmood, X. Jian, Plasma-enhanced interfacial engineering of FeSiAl@PUA@SiO_2 hybrid for efficient microwave absorption and anti-corrosion, Nano Res. 16 (1) (2023) 645–653.
[9] Y. Jia, N. Yang, S. Xu, A.D. Snyder, J.F. Patrick, R. Kumar, D. Zhang, C. Xu, Polymer-derived SiOC reinforced with core–shell nanophase structure of ZrB_2/ZrO_2 for excellent and stable high-temperature microwave absorption (up to 900 °C), Sci. Rep. 13 (1) (2023) 267.
[10] X. Jian, W. Tian, J. Li, L. Deng, Z. Zhou, L. Zhang, H. Lu, L. Yin, N. Mahmood, High-temperature oxidation-resistant $ZrN_{0.4}B_{0.6}$/SiC nanohybrid for enhanced microwave absorption, ACS Appl. Mater. Interfaces 11 (17) (2019) 15869–15880.
[11] X. Yang, Y. Duan, S. Li, H. Pang, L. Huang, Y. Fu, T. Wang, Bio-inspired microwave modulator for high-temperature electromagnetic protection, infrared stealth and operating temperature monitoring, Nano-Micro Lett. 14 (1) (2022) 1–12.
[12] Y. Guo, X. Jian, L. Zhang, C. Mu, L. Yin, J. Xie, N. Mahmood, S. Dou, R. Che, L. Deng, Plasma-induced FeSiAl@Al_2O_3@SiO_2 core–shell structure for exceptional microwave absorption and anti-oxidation at high temperature, Chem. Eng. J. 384 (2020), 123371.
[13] K. Peng, C. Liu, Y. Wu, G. Fang, G. Xu, Y. Zhang, C. Wu, M. Yan, Understanding the efficient microwave absorption for FeCo@ZnO flakes at elevated temperatures a combined experimental and theoretical approach, J. Mater. Sci. Technol. 125 (2022) 212–221.
[14] Z. Jiang, H. Si, Y. Li, D. Li, H. Chen, C. Gong, J. Zhang, Reduced graphene oxide@carbon sphere based metacomposites for temperature-insensitive and efficient microwave absorption, Nano Res. 15 (9) (2022) 8546–8554.
[15] H. Zhang, N. Luo, T. Liu, F. Chen, Q. Fu, Light-weight, low-loading and large-sheet reduced graphene oxide for high-efficiency microwave absorber, Carbon 196 (2022) 1024–1034.
[16] X. Lv, F. Ye, L. Cheng, L. Zhang, 3D printing "wire-on-sphere" hierarchical SiC nanowires/SiC whiskers foam for efficient high-temperature electromagnetic wave absorption, J. Mater. Sci. Technol. 109 (2022) 94–104.
[17] J. Liu, X. Wei, L. Gao, J. Tao, L. Xu, G. Peng, H. Jin, Y. Wang, Z. Yao, J. Zhou, An overview of C-SiC microwave absorption composites serving in harsh environments, J. Eur. Ceram. Soc. 43 (4) (2022) 1237–1254.
[18] J. Li, T. Xu, H. Bai, Z. Shen, Y. Huang, W. Xing, Z. Zhou, Structural modifications and electromagnetic property Regulations of Ti3AlC2 MAX for enhancing microwave absorption through the strategy of Fe doping, Adv. Mater. Interfac. 9 (6) (2022), 2101510.
[19] C. Magnus, D. Cooper, C. Jantzen, H. Lambert, T. Abram, M. Rainforth, Synthesis and high temperature corrosion behaviour of nearly monolithic Ti_3AlC_2 MAX phase in molten chloride salt, Corrosion Sci. 182 (2021), 109193.
[20] H. Li, H. Cao, F. Liu, Y. Li, F. Qi, X. Ouyang, N. Zhao, Microstructure, mechanical and electrochemical properties of Ti_3AlC_2 coatings prepared by filtered cathode vacuum arc technology, J. Eur. Ceram. Soc. 42 (5) (2022) 2073–2083.
[21] X. Li, X. Xie, J. Gonzalez-Julian, J. Malzbender, R. Yang, Mechanical and oxidation behavior of textured Ti_2AlC and Ti_3AlC_2 MAX phase materials, J. Eur. Ceram. Soc. 40 (15) (2020) 5258–5271.
[22] G. Greczynski, L. Hultman, A step-by-step guide to perform x-ray photoelectron spectroscopy, J. Appl. Phys. 132 (1) (2022), 011101.
[23] G. Greczynski, L. Hultman, Reliable determination of chemical state in x-ray photoelectron spectroscopy based on sample-work-function referencing to adventitious carbon: resolving the myth of apparent constant binding energy of the C 1s peak, Appl. Surf. Sci. 451 (2018) 99–103.
[24] B. Liu, H. Zhou, H. Meng, G. Pan, D. Li, Fresh properties, rheological behavior and structural evolution of cement pastes optimized using highly dispersed in situ controllably grown Nano-SiO_2, Cement Concr. Compos. 135 (2023), 104828.
[25] S. Singh, S.K. Singh, P.K. Harijan, S.K. Yadav, A. Kumar, Investigation on the effect of Fe impurity pickups during ball milling and Ni dispersion on the microwave absorption performance of ball milled Fe impurities-Ni/SiC composites, J. Mater. Sci. Mater. Electron. 33 (22) (2022) 17828–17841.
[26] J. Wang, Z. Jia, X. Liu, J. Dou, B. Xu, B. Wang, G. Wu, Construction of 1D heterostructure NiCo@C/ZnO nanorod with enhanced microwave absorption, Nano-Micro Lett. 13 (1) (2021) 175.
[27] B. Wang, Y. Fu, J. Li, T. Liu, Yolk-shelled Co@SiO_2@Mesoporous carbon microspheres: construction of multiple heterogeneous interfaces for wide-bandwidth microwave absorption, J. Colloid Interface Sci. 607 (2022) 1540–1550.
[28] H. Xu, G. Zhang, Y. Wang, Y. Wang, H. Wang, Y. Huang, P. Liu, Heteroatoms-doped carbon nanocages with enhanced dipolar and defective polarization toward light-weight microwave absorbers, Nano Res. 15 (10) (2022) 8705–8713.
[29] S.N. Nesov, V.S. Kovivchak, A.M. Badamshin, Formation of chemical compounds in the surface layers of titanium under the action of a high-power ion beam of nanosecond duration, Nucl. Instrum. Methods Phys. Res. Sect. B Beam Interact. Mater. Atoms 531 (2022) 74–81.
[30] L.Å. Näslund, I. Persson, XPS spectra curve fittings of $Ti_3C_2T_x$ based on first principles thinking, Appl. Surf. Sci. 593 (2022), 153442.
[31] J. Hu, T. Yang, J. Chen, X. Yang, J. Qu, Y. Cai, Efficient solar-driven H_2O_2 synthesis in-situ and sustainable activation to purify water via cascade reaction on ZnIn2S4-based heterojunction, Chem. Eng. J. 430 (2022), 133039.
[32] L. Feng, M. Lv, Q. Qian, R. Luo, B. Huang, The synthesis of high purity Ti_3AlC_2 MAX phase via molten salt method, Adv. Powder Technol. 34 (1) (2023), 103920.
[33] S. Yang, X. Sun, Y. Jiang, S. Wu, D. Zhao, Mechanochemical destruction and mineralization of solid-phase hexabromocyclododecane assisted by microscale zero-valent aluminum, Sci. Total Environ. 824 (2022), 153864.
[34] K. An, S. Zhang, H. Wang, N. Li, Z. Zhang, Y. Liu, Co^0–$Co^{\delta+}$ active pairs tailored by Ga-Al-O spinel for CO_2-to-ethanol synthesis, Chem. Eng. J. 433 (2022), 134606.
[35] H. Yan, X. Dai, K. Ruan, S. Zhang, X. Shi, Y. Guo, H. Cai, J. Gu, Flexible thermally conductive and electrically insulating silicone rubber composite films with BNNS@Al 2 O 3 fillers, Adv. Compos. Hybrid Mater. 4 (2021) 36–50.
[36] X. Zhang, Y. Guo, R. Ali, W. Tian, Y. Liu, L. Zhang, X. Wang, L. Zhang, L. Yin, H. Su, Y. Li, L. Deng, X. Jian, Bifunctional carbon-encapsulated FeSiAl hybrid flakes for enhanced microwave absorption properties and analysis of corrosion resistance, J. Alloys Compd. 828 (2020), 154079.
[37] J. Zhao, J. Zhang, L. Wang, S. Lyu, W. Ye, B.B. Xu, H. Qiu, L. Chen, J. Gu, Fabrication and investigation on ternary heterogeneous MWCNT@TiO_2-C fillers and their silicone rubber wave-absorbing composites, Compos. Appl. Sci. Manuf. 129 (2020), 105714.
[38] C. Xiong, Y. Wu, M. Feng, J. Fang, D. Liu, L. Shen, M.D. Argyle, K.A. Gasem, M. Fan, High thermal stability Si-Al based N-carrier for efficient and stable chemical looping ammonia generation, Appl. Energy 323 (2022), 119519.
[39] Q.Y. Chen, L. Yang, L. Liu, et al., XPS and NMR analyze the combined forms of Pb in Cladophora rupestris subcells and its detoxification, Environ. Sci. Pollut. Control Ser. 29 (38) (2022) 57490–57501.
[40] S. Huang, L. Yu, P. Su, T. Wen, M. Sun, D. Huang, X. Wang, S. Wang, Surface enhanced FRET for sensitive and selective detection of doxycycline using organosilicon nanodots as donors, Anal. Chim. Acta 1197 (2022), 339530.
[41] M.K.A. Ali, H. Xianjun, Improving the heat transfer capability and thermal stability of vehicle engine oils using Al_2O_3/TiO_2 nanomaterials, Powder Technol. 363 (2020) 48–58.
[42] Y. Zhang, X. Tai, J. Zhou, T. Zhai, L. Xu, C. Diao, X. Xie, C. Hou, X. Sun, X. Zhang, Enhanced high-temperature thermal conductivity of the reduced graphene oxide@SiO_2 composites synthesised by liquid phase deposition, Ceram. Int. 48 (6) (2022) 8481–8488.
[43] N. You, X. Liu, Q. Zhang, Y. Xu, J. Wang, S. Wang, Oxygen diffusion kinetics during SiO2/SiC plasma oxidation, Vacuum 207 (2023), 111689.
[44] Q. Li, N. Zhang, Y. Gao, Y. Qing, Y. Zhu, K. Yang, J. Zhu, H. Wang, Z. Ma, L. Gao, Effect of the core-shell structure powders on the microstructure and thermal conduction property of YSZ/Cu composite coatings, Surf. Coating. Technol. 424 (2021), 127658.
[45] Y. Guo, L. Zhang, H. Lu, X. Jian, In situ regulation of microstructure and microwave-absorbing properties of FeSiAl through HNO_3 oxidation, Nanotechnol. Rev. 11 (1) (2022) 147–157.
[46] B. Huang, H. Hu, S. Lim, X.-Z. Tang, X. Huang, Y. Liu, J. Yue, Gradient FeNi-SiO2 films on SiC fiber for enhanced microwave absorption performance, J. Alloys Compd. 897 (2022), 163204.
[47] X. Chen, Y. Wu, W. Gu, M. Zhou, S. Tang, J. Cao, Z. Zou, G. Ji, Research progress on nanostructure design and composition regulation of carbon spheres for the microwave absorption, Carbon 1899 (15) (2022) 617–633.
[48] B. Quan, W. Shi, S.J.H. Ong, X. Lu, P.L. Wang, G. Ji, Y. Guo, L. Zheng, Z.J. Xu, Defect engineering in two common types of dielectric materials for electromagnetic absorption applications, Adv. Funct. Mater. 29 (28) (2019), 1901236.
[49] H. Liang, G. Chen, D. Liu, Z. Li, S. Hui, J. Yun, L. Zhang, H. Wu, Exploring the Ni3d orbital unpaired electrons induced polarization loss based on Ni single-atoms model absorber, Adv. Funct. Mater. (2022), 2212604.
[50] Y.S. Fang, J. Yuan, T.T. Liu, et al., Clipping electron transport and polarization relaxation of $Ti_3C_2T_x$ based nanocomposites towards multifunction, Carbon 201 (2023) 371–380.
[51] Z. Zhang, Z. Xiong, Y. Yao, D. Wang, Z. Yang, P. Zhang, Q. Zhao, W. Zhou, Constructing conductive network in hybrid perovskite for a highly efficient microwave absorption system, Adv. Funct. Mater. 32 (39) (2022), 2206053.
[52] H. Liang, L. Zhang, H. Wu, Exploration of twin-modified grain boundary engineering in metallic copper predominated electromagnetic wave absorber, Small 18 (38) (2022), 2203620.

[53] P. Liu, Y. Wang, G. Zhang, Y. Huang, R. Zhang, X. Liu, X. Zhang, R. Che, Hierarchical engineering of double-shelled nanotubes toward hetero-interfaces induced polarization and microscale magnetic interaction, Adv. Funct. Mater. 32 (33) (2022), 2202588.
[54] M. Tang, J.Y. Zhang, S. Bi, et al., Ultrathin topological insulator absorber: unique dielectric behavior of Bi_2Te_3 nanosheets based on conducting surface states, ACS Appl. Mater. Interfaces 11 (36) (2019) 33285–33291.
[55] M. Sun, D. Wang, Z. Xiong, Z. Zhang, L. Qin, C. Chen, F. Wu, P. Liu, Multi-dimensional Ni@C-CoNi composites with strong magnetic interaction toward superior microwave absorption, J. Mater. Sci. Technol. 130 (2022) 176–183.
[56] V. Lalan, S. Ganesanpotti, The smallest anions, induced porosity and graphene interfaces in $C_{12}A_7$: e^- electrides: a paradigm shift in electromagnetic absorbers and shielding materials, J. Mater. Chem. C 10 (3) (2022) 969–982.
[57] G. Dai, R. Deng, T. Zhang, Y. Yu, L. Song, Quantitative evaluation of loss capability for in situ conductive phase enhanced microwave absorption of high-entropy transition metal oxides, Adv. Funct. Mater. 32 (35) (2022), 2205325.
[58] Z. Chen, Y. Zhang, Z. Wang, Y. Wu, Y. Zhao, L. Liu, G. Ji, Bioinspired moth-eye multi-mechanism composite ultra-wideband microwave absorber based on the graphite powder, Carbon 201 (2023) 542–548.